Investigation of a Smooth Local Correlation-based Transition Model in a Discrete-Adjoint Aerodynamic Shape Optimization Algorithm

Michael G. H. Piotrowski*
NASA Ames Research Center, Moffett Field, CA 94035
Institute for Aerospace Studies, University of Toronto, ON M3H 5T6

David W. Zingg†
Institute for Aerospace Studies, University of Toronto, ON M3H 5T6

A smooth local correlation-based transition model is fully coupled to a RANS-based Newton-Krylov flow solver and discrete-adjoint gradient-based optimization algorithm. The free-transition optimization framework is evaluated using lift-constrained drag minimizations of airfoils at design conditions ranging from light to single-aisle aircraft and an infinite swept wing at design conditions representative of a transonic strut-braced wing aircraft. The impact of the streamwise grid resolution on the ability of the optimization algorithm to delay boundary-layer transition is investigated, with the results demonstrating that streamwise grid resolution requirements increase as the transition length decreases with increasing Reynolds number. The optimization problem at the light aircraft design conditions is demonstrated to be multi-modal, with the optimization algorithm producing two distinct designs: one with a thin, reflexed trailing edge and steep pressure recovery regions, the other with increased aft loading, with the latter design outperforming the former. A drag minimization of an airfoil at transonic design conditions demonstrates that the optimization algorithm successfully trades a decrease in viscous drag by delaying boundary-layer transition with an increase in wave drag, while the drag minimization of an infinite swept wing demonstrates the capability of the optimization algorithm to delay both Tollmien-Schlichting and stationary crossflow instabilities.

I. Introduction

Laminar-flow wing designs produce an increased laminar extent of the boundary layer, resulting in a decrease in viscous drag [1]. These drag savings have the potential to significantly reduce the fuel burn of transport aircraft, where viscous drag constitutes approximately 50% of the total drag [2]. The potential of laminar-flow designs has been demonstrated by various studies which suggest the application of laminar flow control to large commercial aircraft can reduce aerodynamic drag by approximately 10% [3].

In the near term, natural laminar flow (NLF) is being investigated for winglet, tail, and nacelle designs, with the Boeing 787-8 and 777X representing the first commercial applications of NLF nacelles to large transport aircraft, and the 737 Max aircraft exploiting laminar flow for both the nacelle and winglet designs [4]. In the future, the design of wings which exploit significant regions of laminar flow can result in more significant drag reduction. The Airbus BLADE project is investigating this, while experimental studies of the NASA common research model NLF (CRM-NLF) demonstrate that it is possible to design transport wings with high sweep and Reynolds numbers with significant regions of laminar flow [5–7].

Efficient high-fidelity numerical optimization algorithms provide the designers of next generation aircraft with powerful tools for the development of more fuel-efficient designs [8–11]. The integration of transition prediction methodologies into aerodynamic shape optimization algorithms enables the study of various trade-offs in the design of novel NLF wing configurations. Although there are several examples in the literature of researchers combining transition prediction with aerodynamic optimization using lower-fidelity models [12–17], or with gradient-free or costly

*NASA Pathways Ph.D. Candidate, University of Toronto, NASA Computational Aeroscience Branch, AIAA Student Member, m.piotrowski@mail.utoronto.ca

†University of Toronto Distinguished Professor of Computational Aerodynamics and Sustainable Aviation, Associate Fellow AIAA, dwz@oddjob.utias.utoronto.ca

finite-difference gradient approximations [18–24], the focus of the current review will be limited to methods using RANS-based analysis with adjoint-based shape optimization algorithms.

The work by Driver and Zingg [25] represents an early example of the use of RANS-based optimization to investigate the design of NLF airfoils. The coupled inviscid-viscous boundary-layer solver MSES [26] was used to calculate transition locations, which were enforced using the trip terms in the Spalart-Allmaras (SA) turbulence model [27]. Through the application of the resulting algorithm to single-point optimizations, Driver and Zingg [25] produced NLF airfoil designs with laminar-flow design characteristics similar to those designed by Liebeck [28] and Zingg [29].

Lee and Jameson [30] coupled a boundary-layer solver and database e^N method, developed by Kroo and Sturdza [16] for the design of supersonic laminar flow wings, to the Baldwin-Lomax algebraic turbulence model [31] in a RANS-based solver and discrete-adjoint gradient-based optimization algorithm. Although their work demonstrated the significance of laminar flow on NLF wing design, the gradients did not include transition prediction. Instead, the optimizations were focused on reducing wave drag in order to increase aerodynamic performance.

Rashad and Zingg [32] performed single- and multi-point optimizations at subsonic and transonic design conditions using the simplified e^N envelope method developed by Drela and Giles [26] coupled to the SA turbulence model [27]. Rashad conducted a thorough investigation of coupling strategies for the RANS-e^N flow solver and demonstrated the importance of providing a smooth ramp-up of the eddy-viscosity, as well as using a tight tolerance for the transition residual, in order to ensure a smooth design space [32, 33]. The coupled-adjoint system is solved using preconditioned GMRES with a non-iterative solution strategy. Single-point optimizations demonstrate that the resulting algorithm is capable of extending the laminar boundary layer significantly, with multi-point optimizations producing NLF airfoil designs robust to changes in the flow conditions and disturbance environments. The drag minimizations performed by Rashad and Zingg [32] represent suitable two-dimensional reference benchmarks for evaluating NLF optimization frameworks.

Shi et al. [34] used a simplified e^N method based on a database of linearized stability theory (LST) results in a Jacobian-free discrete-adjoint optimization algorithm. Similar to the work by Rashad [33] and Rashad and Zingg [32], Shi et al. [34] emphasized the importance of using a smooth intermittency function to couple the simplified e^N method with the RANS solutions, as well as a tight transition residual tolerance. Shi et al. investigated single-point airfoil optimizations at the Cessna 172R design conditions initially proposed by Rashad and Zingg [32], producing an optimized NLF design similar to that developed by Rashad and Zingg, and multi-point optimizations of an airfoil at design conditions representative of the HondaJet aircraft [35]. Their work was recently extended to infinite swept wing optimizations using the C1 criterion [36].

Zhu and Qin [37] applied the simplified e^N envelope method by Drela and Giles [26], extended with the crossflow criterion developed by Kroo and Sturdza [16], and using Poll's criterion [38] as a constraint to prevent attachment-line transition, to the optimization of infinite swept wings using a discrete-adjoint optimization algorithm. Similar to Lee and Jameson [30], the transition locations from stability analysis were enforced using the Baldwin-Lomax algebraic turbulence model [31]. Drag-minimizations of infinite swept wings at transonic flight conditions were performed both with and without a shock-control bump. The shock-control bump reduces wave drag, enabling the optimization algorithm to reduce sweep, which attenuates the crossflow instabilities, moving the transition front downstream. A systems-level benefit assessment was performed demonstrating that a low-sweep NLF wing design with shock-control bumps applied to a narrow-body commercial aircraft can reduce fuel consumption by 11.1% [39].

Methods based on stability analysis require non-local boundary-layer information and a large infrastructure to apply the code, usually consisting of a boundary-layer solver and an e^N method. While previous work has successfully demonstrated that methods for automatic transition prediction using stability analysis can be developed for complex three-dimensional configurations [40, 41], methods based on local transition criteria, such as the Langtry-Menter transition model (LM2009) [42], can be more easily integrated into a RANS-based flow solver and gradient-based optimization algorithm.

Khayatzadeh and Nadarajah [43, 44] coupled the Langtry-Menter LM2009 transition model [42] with a RANS-based flow solver and discrete-adjoint optimization algorithm. Through the application of the resulting algorithm to subsonic lift-constrained drag-minimization and lift-to-drag ratio maximization optimizations, they demonstrated the importance of fully coupling the transition model equations to the adjoint system, and successfully produced designs that delayed the onset of transition.

Halila et al. [45] integrated a smooth version of the amplification factor transport (AFT) transition model [46], coupled to the SA turbulence model, with an approximate Newton-Krylov flow solver and discrete-adjoint optimization algorithm. The resulting algorithm was applied to single- and multi-point subsonic and single-point transonic airfoil drag minimizations.

Yang and Mavriplis [47] integrated the AFT transition model [46] with a Newton-Krylov flow solver and discrete-adjoint framework and applied the algorithm to two-dimensional subsonic optimizations. Following this work, Mavripilis et al. [48] applied the one-equation intermittency transition model developed by Menter et al. [49], coupled to the SA turbulence model [27], in a discrete-adjoint optimization algorithm to a slotted transonic truss-braced wing (TTBW) geometry.

In general, optimized designs resulting from algorithms combining gradient-based optimization with local transport-equation-based transition models tend to underperform NLF designs produced using stability-analysis approaches coupled with gradient-based optimization algorithms. Specifically, gradient-based optimization algorithms with transport-equation-based transition models struggle to produce designs with significantly increased regions of laminar flow [43, 44, 47, 50], especially at higher Mach and Reynolds numbers [45]. This is particularly evident when comparing with the designs produced by Rashad and Zingg [32] that achieve significant regions of laminar flow at high Mach numbers and flight-scale Reynolds numbers.

The goal of this work it to evaluate the capabilities of a discrete-adjoint gradient-based optimization algorithm coupled with a smooth local correlation-based transition model. To achieve this goal, the SA-sLM2015 transition model [51–53] is fully coupled into a RANS-based Newton-Krylov flow solver [51, 53] and discrete-adjoint gradient-based optimization algorithm, with details and verification of the gradients of the resulting algorithm presented in Section II. The free-transition optimization framework is investigated using airfoil drag minimizations at design conditions ranging from subsonic, representative of light aircraft, up to transonic conditions representative of single-aisle aircraft, and an infinite swept wing drag minimization at design conditions representative of a transonic strut-braced wing aircraft. The influence of the streamwise resolution of the grids and constraints applied to the design space on the behaviour of the optimization algorithm is investigated, with the results presented in Section III. Conclusions and future work are presented in Section IV.

II. Methodology

The high-fidelity discrete-adjoint gradient-based aerodynamic shape optimization framework used in the current work, Jetstream, consists of three primary components: a geometry parameterization and control scheme [54–56], a parallel structured multi-block Newton-Krylov-Schur RANS-based flow solver [51, 53, 57, 58], and a discrete-adjoint gradient-based optimization algorithm [54, 59]. Jetstream was recently cross-validated with an industry RANS-based discrete-adjoint optimization algorithm, with the two algorithms producing very similar geometries and performance improvements [60]. The flow solver, Diablo, was extensively validated with fully-turbulent flow as part of the Fifth AIAA Drag Prediction Workshop [61], and has recently been extended to perform free-transition simulations using the SA-sLM2015 transition model in subsonic and transonic flow regimes [51–53]. This section will provide an overview of these components with an emphasis on the flow solver and gradient evaluation, which were modified for the introduction of the SA-sLM2015 transition model equations.

A. Flow Solution Algorithm

The flow solution algorithm used in the current work is a three-dimensional structured multi-block finite-difference solver [57, 58] which solves the RANS equations fully-coupled to the three-equation SA-sLM2015 transition model [51–53]. The governing equations are spatially discretized using summation-by-parts operators, with simultaneous approximation terms applied to enforce boundary conditions and inter-block coupling. The mean-flow equations are discretized using second-order summation-by-parts operators with artificial dissipation provided using the matrix-based dissipation model developed by Swanson and Turkel [62]. First-order upwinding is applied to the turbulence and transition model equations. The computational domain is decomposed into multiple blocks, resulting in multi-block structured grids, which allow for efficient parallel computations. A fully-coupled, implicit Newton-Krylov-Schur solution algorithm making use of a pseudo-transient continuation strategy is applied to the set of discretized equations to drive the residual to a converged steady-state solution. Details of the modifications made to the Newton-Krylov-Schur algorithm to integrate the transition model equations can be found in [51, 53].

The work by Rashad [33] and Rashad and Zingg [32] emphasizes the importance of ensuring a smooth design space for gradient-based optimization. However, many local transport-based transition models [42, 46, 49, 63] contain discontinuous and non-differentiable functions. In previous work, the current authors developed the smooth, three-equation SA-sLM2015 transition model [51], which is based on the LM2009 [42] empirical correlations for bypass transition and transition due to Tollmien-Schlichting instabilities as well as the LM2015 [64] helicity-based empirical correlations for stationary crossflow instabilities. The empirical correlations in the SA-sLM2015 transition model were recently extended to transonic flow regimes [52].

B. Gradient-based Optimization

1. Optimization Algorithm

The optimization algorithm consists of an integrated geometry parametrization and mesh movement scheme developed by Hicken and Zingg [54] that represents the initial geometry by a set of B-spline surface patches. Shape control is achieved using free-form deformation (FFD) B-spline volumes with an axial deformation geometry control system [55, 56]. Optimization is performed using a gradient-based optimization strategy where the gradients are calculated using the discrete-adjoint approach [54, 59]. The flow adjoint system is solved using a simplified and flexible variant of GCROT [65], while the mesh adjoint system is solved using a preconditioned conjugate-gradient method. The design variables are updated using the sparse quadratic programming algorithm SNOPT [66], which is capable of handling both linear and non-linear constraints and has been demonstrated to be efficient for problems with large numbers of design variables.

2. Gradient Evaluation

The discrete-adjoint Lagrangian function for the PDE-constrained optimization problem containing the flow, $\boldsymbol{\psi}_{\mathrm{f}}$, and mesh adjoint variables, $\boldsymbol{\psi}_{\mathrm{m}}$, is given by,

$$L(\boldsymbol{Q}, \boldsymbol{C}, \boldsymbol{X}, \boldsymbol{\psi}_{\mathrm{f}}, \boldsymbol{\psi}_{\mathrm{m}}) = J(\boldsymbol{Q}, \boldsymbol{C}, \boldsymbol{X}) - \boldsymbol{\psi}_{\mathrm{f}}^T (\boldsymbol{R}(\boldsymbol{Q}, \boldsymbol{C}, \boldsymbol{X})) - \boldsymbol{\psi}_{\mathrm{m}}^T \boldsymbol{M}(\boldsymbol{C}, \boldsymbol{X}), \tag{1}$$

where $\boldsymbol{Q}$, $\boldsymbol{C}$, and $\boldsymbol{X}$ represent the array of conserved flow variables, B-spline control points, and design variables, and $\boldsymbol{R}$ and $\boldsymbol{M}$ represent the total residual, which includes the RANS, turbulence, and transition model equations, and the mesh movement equations, respectively. Setting the first derivatives of the Lagrangian with respect to $\boldsymbol{Q}$, $\boldsymbol{C}$, $\boldsymbol{X}$, $\boldsymbol{\psi}_{\mathrm{f}}$, and $\boldsymbol{\psi}_{\mathrm{m}}$ to zero, we recover the following first-order optimality conditions,

$$\frac{\partial L}{\partial \boldsymbol{\psi}_{\mathrm{m}}} = 0 = \boldsymbol{M}(\boldsymbol{C}, \boldsymbol{X}), \tag{2}$$

$$\frac{\partial L}{\partial \boldsymbol{\psi}_{\mathrm{f}}} = 0 = \boldsymbol{R}(\boldsymbol{Q}, \boldsymbol{C}, \boldsymbol{X}), \tag{3}$$

$$\frac{\partial L}{\partial \boldsymbol{Q}} = 0 = \frac{\partial J}{\partial \boldsymbol{Q}} - \boldsymbol{\psi}_{\mathrm{f}}^T \frac{\partial \boldsymbol{R}}{\partial \boldsymbol{Q}}, \tag{4}$$

$$\frac{\partial L}{\partial \boldsymbol{C}} = 0 = \frac{\partial J}{\partial \boldsymbol{C}} - \boldsymbol{\psi}_{\mathrm{f}}^T \frac{\partial \boldsymbol{R}}{\partial \boldsymbol{C}} - \boldsymbol{\psi}_{\mathrm{m}}^T \frac{\partial \boldsymbol{M}}{\partial \boldsymbol{C}}, \tag{5}$$

$$\frac{\partial L}{\partial \boldsymbol{X}} = 0 = \frac{\partial J}{\partial \boldsymbol{X}} - \boldsymbol{\psi}_{\mathrm{f}}^T \frac{\partial \boldsymbol{R}}{\partial \boldsymbol{X}} - \boldsymbol{\psi}_{\mathrm{m}}^T \frac{\partial \boldsymbol{M}}{\partial \boldsymbol{X}}, \tag{6}$$

where in the current work the partial derivatives are formed analytically using hand linearization with some entries determined using the complex-step method.

To perform free-transition optimization, the partial derivatives of the total residual must be updated. Specifically, the flow Jacobian, $\frac{\partial \boldsymbol{R}}{\partial \boldsymbol{Q}}$, and metric linearization, $\frac{\partial \boldsymbol{R}}{\partial \boldsymbol{C}}$, used for the flow and mesh adjoint systems (Equations 4 and 5), respectively, are updated to include the modifications to the SA turbulence model and the transition model equations, enabling free-transition gradient-based aerodynamic shape optimization. Because these partial derivatives are formed analytically it is important to verify their implementation. The analytical flow Jacobian and metric linearization are each verified through comparing with the complex-step method, while the analytical gradient is verified using a second-order finite-difference approximation. It is important to note that the axial and FFD geometric design variables are formed using the B-spline control points, $\boldsymbol{C}$, [55] and that the residuals depend on the B-spline control points through the grid metrics and the off-wall spacing, the latter of which is used in the turbulence and transition model source terms. Furthermore, partial derivatives involving the angle of attack and sideslip design variables are determined using the complex-step method. Therefore, the analytical $\frac{\partial \boldsymbol{R}}{\partial \boldsymbol{X}}$ is verified concurrently with $\frac{\partial \boldsymbol{R}}{\partial \boldsymbol{C}}$.

It is important that the verification tests include all relevant flow features. To ensure this, an infinite swept wing geometry consisting of a blunt trailing-edge RAE2822 airfoil extruded with a 25 degree sweep and periodic boundary conditions is simulated using the smooth transition model with the local helicity-based crossflow correlations and compressibility corrections, SA-sLM2015cc, presented in [52]. The infinite swept wing is simulated at a Mach number

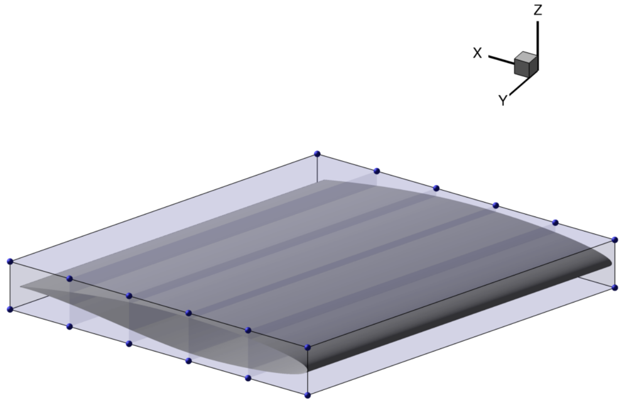

Fig. 1 Infinite swept wing geometry with FFD design variables in blue.

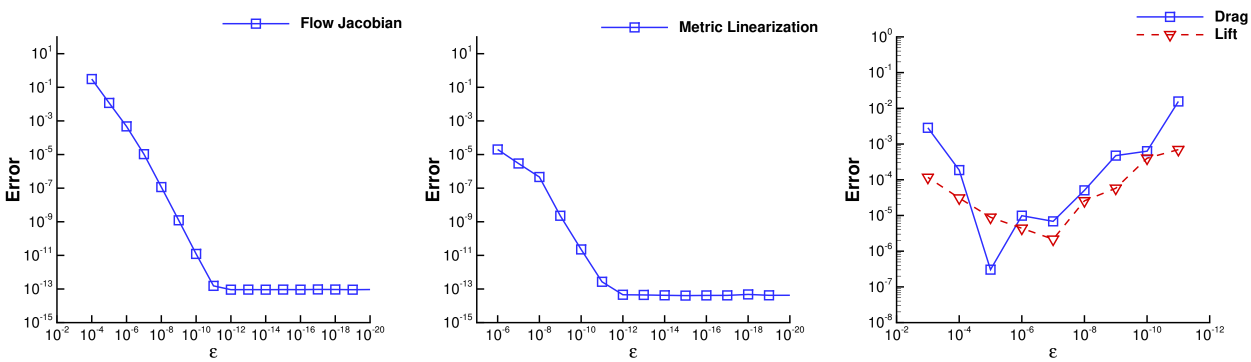

(a) Flow Jacobian: $\frac{\partial R}{\partial Q}$ **(b) Metric Linearization: $\frac{\partial R}{\partial C}$** **(c) Directional Derivative: $D_{\mathbf{z}}J$**

Fig. 2 Verification for the analytical flow Jacobian, metric linearization, and directional derivative including the SA-sLM2015cc transition model equations using both complex-step and finite-difference approximations.

of 0.785, Reynolds number of 20.3×10^6, lift coefficient of 0.56, turbulence intensity of 0.07%, and with an assumed surface roughness of 1.8μm. The infinite swept wing O-grid consists of 561, 121, and 11 nodes in the streamwise, off-wall, and spanwise directions, respectively, with average and maximum $y+$ values of 0.25 and 0.50. The geometry is parameterized using B-spline surface patches that are embedded in an FFD volume with 6 FFD design variables on each of the upper and lower surfaces, as presented in Figure 1. The design variables are constrained to be constant along the span and the leading- and trailing-edge design variables are constrained to move symmetrically, resulting in 10 effective geometric design variables plus angle of attack. Although the current test does not involve axial control system design variables, the two-level axial and FFD control system was not modified by the inclusion of the transition model equations. The changes to the partial derivatives that were made to enable free-transition optimization can be verified by considering only the FFD geometric design variables and angle of attack.

The verification cases are performed using a fully-converged SA-sLM2015cc simulation on the infinite swept wing to ensure that the turbulence and transition model source terms are active. The results for the verification study are presented in Figure 2. Machine-zero agreement is demonstrated for both the analytical flow Jacobian and metric linearization with approximations formed using the complex-step method. A directional derivative is used to verify the analytical gradient components simultaneously [67, 68], defined as,

$$D_{\mathbf{z}}J = \frac{\partial J}{\partial X}\mathbf{z}, \tag{7}$$

and the second-order finite-difference approximation is,

$$D_{\mathbf{z}}J = \frac{J(X + \epsilon\mathbf{z}) - J(X - \epsilon\mathbf{z})}{2\epsilon} + O(\epsilon^2), \tag{8}$$

Table 1 Design conditions for the two-dimensional lift-constrained drag minimizations [32]. For each case turbulence intensity, Tu, is specified as 0.07%.

design condition	lift coefficient	Mach number	Reynolds number (MAC)
Cessna 172R	0.30	0.19	5.6×10^6
De Havilland Dash8-Q400	0.42	0.60	15.7×10^6
Boeing 737-800	0.50	0.71 (corr.)	20.3×10^6

where ϵ is the perturbation parameter. The difference between the values produced by the analytical directional derivative and the second-order finite-difference approximation is presented in Figure 2c. Good agreement is demonstrated to approximately 6 and 7 orders of magnitude with the objective function set to lift and drag, respectively. Figure 2c demonstrates increased round-off error with large step sizes, which is a consequence of using a finite-difference approximation.

III. Results

In this section, the free-transition optimization framework presented in Section II is applied to single-point lift-constrained drag minimizations of airfoils and an infinite swept wing geometry. Airfoil optimizations are performed using an initial geometry based on a blunt trailing-edge RAE2822 airfoil. For the infinite swept wing optimization, the airfoil is extruded one chord length with 11 nodes in the spanwise direction and with periodic boundary conditions applied at the wing root and tip. The airfoil and wing surfaces are parameterized using B-spline surface patches, which are controlled using FFD design variables. For the results presented, 6 streamwise FFD design variables are applied to each of the upper and lower surfaces, with the infinite swept wing root and tip design variables constrained to be equal and the leading- and trailing-edge design variables constrained to move symmetrically, for a total of 10 effective geometric design variables plus angle of attack.

A. Airfoil Optimization

For the two-dimensional airfoil optimizations, three design conditions are considered that are representative of aircraft classes ranging from light aircraft up to single-aisle aircraft based on the work of Rashad and Zingg [32], as presented in Table 1. The Cessna 172R and De Havilland Dash8-Q400 aircraft have nominally zero sweep; however, the Boeing 737-800 design Mach number is corrected from a cruise Mach number of 0.785 to an effective Mach number of 0.71 based on a wing sweep of 25 degrees. Although the two-dimensional Boeing 737-800 design condition does not include the effects of crossflow instabilities, and therefore is not representative of the disturbance environment for a single-aisle aircraft wing, drag minimizations at these design conditions are valuable for investigating the streamwise grid resolution requirements for NLF optimizations at large Mach and Reynolds numbers, as well as for comparing the optimized designs with designs previously developed by Rashad and Zingg [32]. A drag minimization of an infinite swept wing that includes the effects of both Tollmien-Schlichting and stationary crossflow instabilities is investigated in Section III.B.

1. Cessna 172R Skyhawk

Preliminary optimizations revealed that the capability of the optimization algorithm to delay the onset of boundary-layer transition when applied to free-transition design problems was sensitive to the streamwise resolution of the grid. To investigate this further, three structured multi-block O-type topology grids with varying levels of streamwise grid resolution were considered for the Cessna 172R drag minimizations, with the grid details presented in Table 2. Lift-constrained drag minimizations are performed at each grid level with the cross-sectional area of the airfoil constrained so that it cannot decrease and with loose thickness-to-chord ratio constraints enforced at each FFD design variable pair. The optimization problem, which will be referred to as the baseline optimization problem, is given by,

$$\min_{\boldsymbol{X}} \quad C_d(\boldsymbol{Q}, \boldsymbol{X}), \tag{9}$$

$$\text{s.t.} \quad C_l = C_l^*, \tag{10}$$

$$A \geq A_{\text{init}}, \tag{11}$$

Table 2 Structured multi-block O-grid dimensions for the two-dimensional optimizations at the Cessna 172R design conditions (see Table 1).

grid level	chord x off-wall nodes	avg/max $\Delta s \times 10^{-6}$ (chord)	avg/max $y+$
L0	281x121	1.09 / 1.19	0.17 / 0.54
L1	561x121	"	"
L2	1121x121	"	"

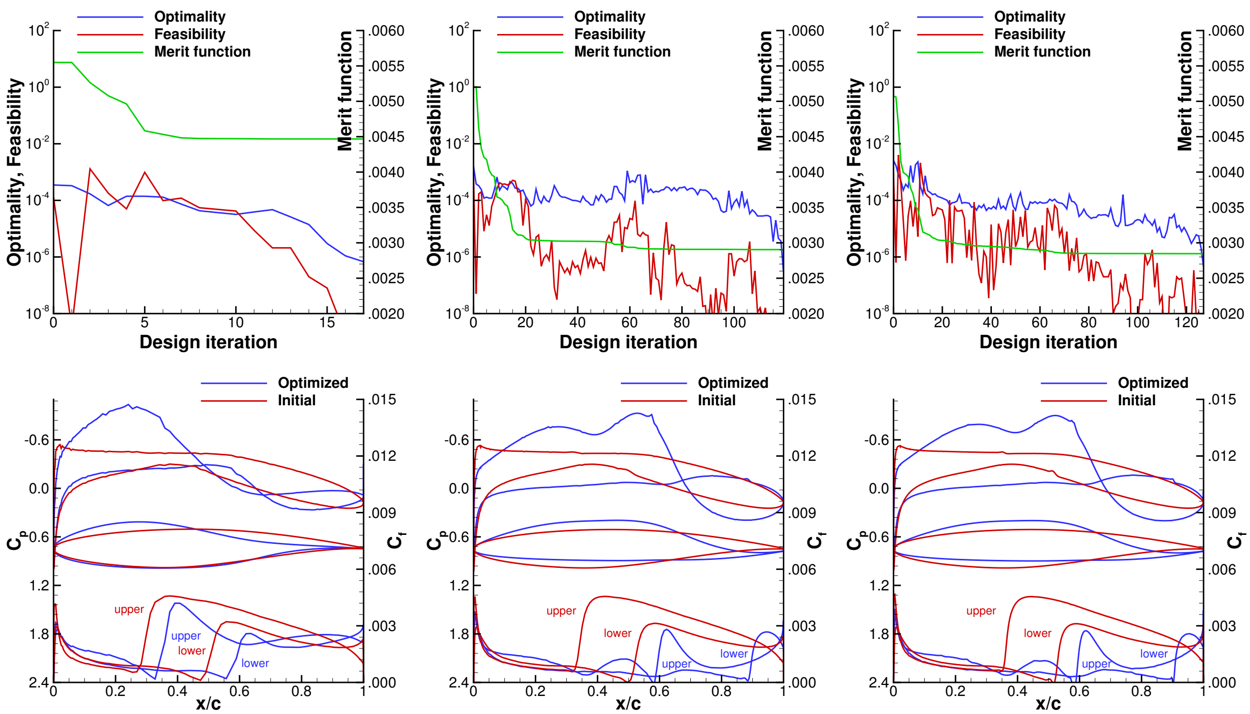

(a) L0 (b) L1 (c) L2

Fig. 3 Optimization convergence histories and cross-sectional profiles of the initial and optimized designs produced by drag minimizations with the baseline optimization problem (Equations 9-12) at the Cessna 172R conditions with varying streamwise grid resolution.

$$t/c \geq 0.15 t/c_{\text{init}}, \tag{12}$$

where the vectors of solution and design variables are represented by $\boldsymbol{Q}$ and $\boldsymbol{X}$, respectively, and C_l^* represents the design lift coefficient presented in Table 1.

The results from the baseline drag minimizations are presented in Figure 3. The results suggest that the large gradients in the transition region can be under-resolved due to poor streamwise grid resolution. Instead of delaying transition, the results in Figure 3a demonstrate that for the L0 grid level the optimization algorithm generates significant adverse pressure gradients downstream of the transition locations by reducing the trailing-edge thickness, where the flow deceleration reduces the turbulent skin friction coefficient and skin friction drag. This behaviour is also produced in the Dash8-Q400 optimizations presented in the following section (Figure 5a). The optimization algorithm produces more efficient designs with larger extents of laminar flow as the streamwise resolution of the grid is increased. Figure 3 illustrates that at the L1 grid level the optimization algorithm is able to delay the onset of boundary-layer transition on both surfaces significantly. Diminishing returns are encountered by doubling the streamwise resolution going from the L1 to the L2 grid level, which provides a modest reduction in drag but significantly increases the computational cost of the optimizations.

The optimized designs in Figures 3b and 3c feature concave pressure recovery regions on the airfoil upper surface

Table 3 Aerodynamic performance of the initial and optimized designs at the Cessna 172R conditions on the L1 grid level.

	C_d (cnts.)	C_l	C_m	L/D	aoa (deg.)
Initial	52.04	0.30	-0.060	57.647	0.971
Baseline Optimization Problem	29.04	0.30	0.034	103.294	2.542
Additional Constraints	28.88	0.30	-0.060	103.872	0.551
Re-optimized w/ Baseline Optimization Problem	27.75	0.30	-0.058	108.127	0.600

and extended regions of favourable pressure gradient on the lower surface. Instead of a flat pressure plateau on the upper surface, the optimization algorithm has produced a flow deceleration section followed by flow acceleration. The optimization algorithm has achieved these designs by increasing the angle of attack, decreasing the trailing-edge thickness, and moving the aerodynamic loading upstream. However, from a manufacturability standpoint the thin trailing edge is undesirable. Furthermore, the design features a reflexed trailing edge that reduces lift in order to satisfy the target lift coefficient, and steep adverse pressure gradients that could reduce the performance of the airfoil at higher angles of attack. Rashad and Zingg [32] produced a more optimal design at the same design conditions using a discrete-adjoint optimization algorithm coupled with a stability-analysis framework that features more aft-loading with increased trailing-edge thickness. To investigate whether the optimization algorithm can recover a geometry similar to that of Rashad and Zingg [32] and to address the undesirable characteristics mentioned above, the optimization problem was modified to include a pitching-moment constraint and more conservative thickness-to-chord ratio constraints. The optimization problem with the additional constraints is presented below,

$$\min_{\boldsymbol{X}} \quad C_d(\boldsymbol{Q}, \boldsymbol{X}), \tag{13}$$

$$\text{s.t.} \quad C_l = C_l^*, \tag{14}$$

$$C_m = C_{m,\text{init}}, \tag{15}$$

$$A \geq A_{\text{init}}, \tag{16}$$

$$t/c \geq 0.85 t/c_{\text{init}}. \tag{17}$$

Based on the results from the streamwise grid-resolution study presented in Figure 3, the drag minimization with the optimization problem with additional constraints is performed on the L1 grid level. The results from the drag minimizations with the baseline and more constrained optimization problems are presented in Figure 4. The optimization with the more constrained optimization problem (Equations 13-17) produces a design with extended regions of near-zero pressure gradient on both the upper and lower surfaces of the airfoil that delay boundary-layer transition and increase the laminar extent of the boundary layer. The optimization algorithm produces this design by maintaining more aft-loading relative to the baseline optimized design, with the new design also featuring increased trailing-edge thickness. The resulting design closely resembles the design produced by the lift-constrained drag minimization performed by Rashad and Zingg [32]. Moreover, the optimization history demonstrates that the design produced by the optimization with additional constraints produces lower drag than the design produced by the baseline optimization problem, despite lying in the design space of the latter. The results suggest that the Cessna 172R design space is multi-modal, with the optimization algorithm producing (at least) two distinct local minima. Details of the aerodynamic performance of the initial blunt trailing-edge RAE2822 airfoil and the two optimized designs are presented in Table 3.

To confirm that the optimized design produced using the additional constraints is a local minimum in the baseline optimization problem design space, the more constrained optimized design was used as an initial geometry with the relaxed constraints of the baseline optimization problem. The results in Figure 4c and Table 3 demonstrate that the optimization algorithm is able to reduce drag by an additional count by decreasing the trailing-edge thickness to create stronger adverse pressure gradients near the trailing edge, which reduce the skin friction in the turbulent boundary layer. However, the new design maintains a similar profile to the initial design produced with the additional constraints. The results in Figure 4c and Table 3 confirm that the Cessna 172R design space has at least two distinct local minima, one with a higher design angle of attack and extended regions of laminar flow on the lower surface of the airfoil and one with more aft-loading and more balanced extents of laminar flow on the upper and lower surfaces, with the latter outperforming the former. The results demonstrate the significant risk multimodality presents at these design conditions,

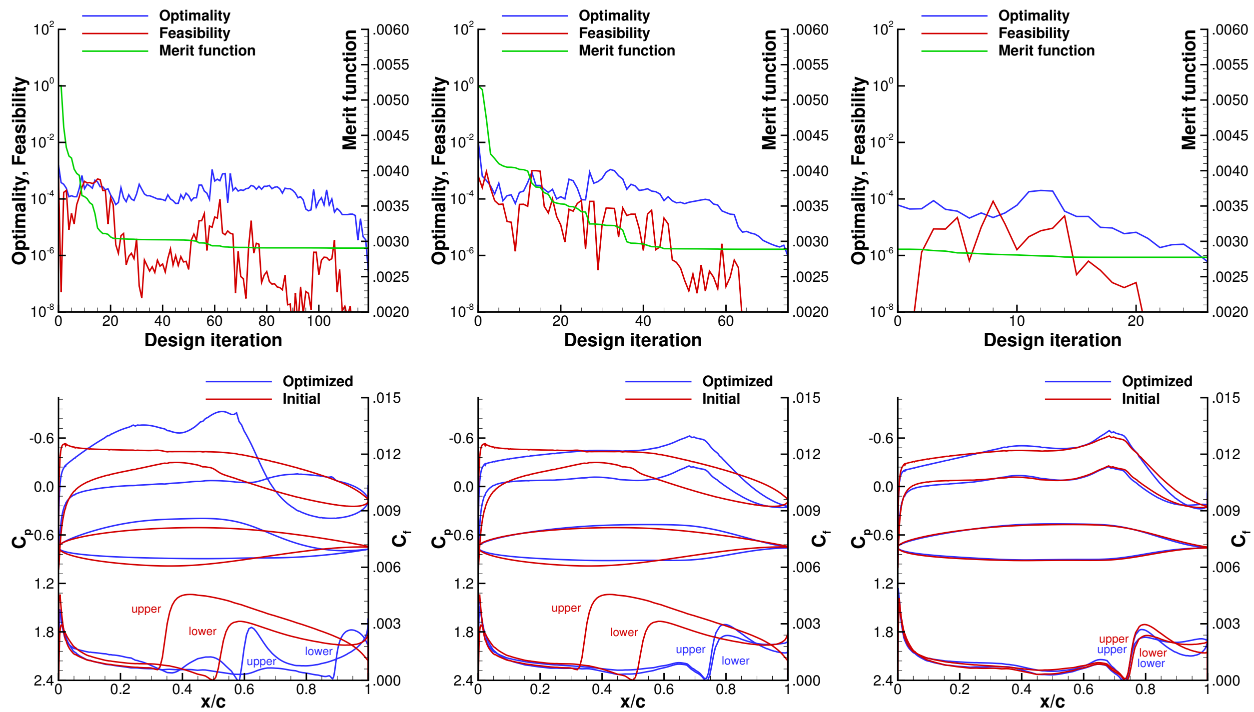

(a) Baseline Optimization Problem

(b) Additional Constraints

(c) Re-optimized w/ Baseline Optimization Problem

Fig. 4 Optimization convergence histories and cross-sectional profiles of the initial and optimized designs produced by drag minimizations with the baseline (Equations 9-12) and more constrained optimization problem (Equations 13-17) at the Cessna 172R conditions on the L1 grid level.

Table 4 Structured multi-block O-grid dimensions for the two-dimensional optimizations at the Dash8-Q400 design conditions (see Table 1).

grid level	chord x off-wall nodes	avg/max $\Delta s \times 10^{-6}$ (chord)	avg/max $y+$
L1	561x121	0.65 / 0.74	0.26 / 0.53
L2	1121x121	"	"

as the baseline optimization problem produces an inferior design, and highlights the importance of efficient global optimization techniques, such as gradient-based multistart methods [69, 70].

2. De Havilland Dash8-Q400

Based on the results from the Cessna 172R drag minimizations, grids with streamwise resolutions representative of the L1 and L2 grid levels are investigated for the drag minimizations at the higher Mach and Reynolds numbers of the Dash8-Q400 design conditions. The Dash8-Q400 design conditions are presented in Table 1, with the grid details for the L1 and L2 grid levels presented in Table 4. Similar to the Cessna 172R case, a streamwise grid-resolution study is performed using the L1 and L2 grids and the baseline optimization problem (Equations 9-12) in order to evaluate the capabilities of the optimization algorithm to explore the Dash8-Q400 design space. The optimization histories and cross-sectional profiles for the initial and optimized designs are presented in Figure 5.

The results demonstrate that there is a significant difference in both airfoil profile shape and performance of the designs produced by the optimization algorithm on the L1 and L2 grid levels. Where the L1 grid level provides adequate resolution for the lower Reynolds number drag minimizations at the Cessna 172R design conditions, the optimizations at the higher Mach and Reynolds numbers of the Dash8-Q400 design conditions require finer streamwise grid resolutions.

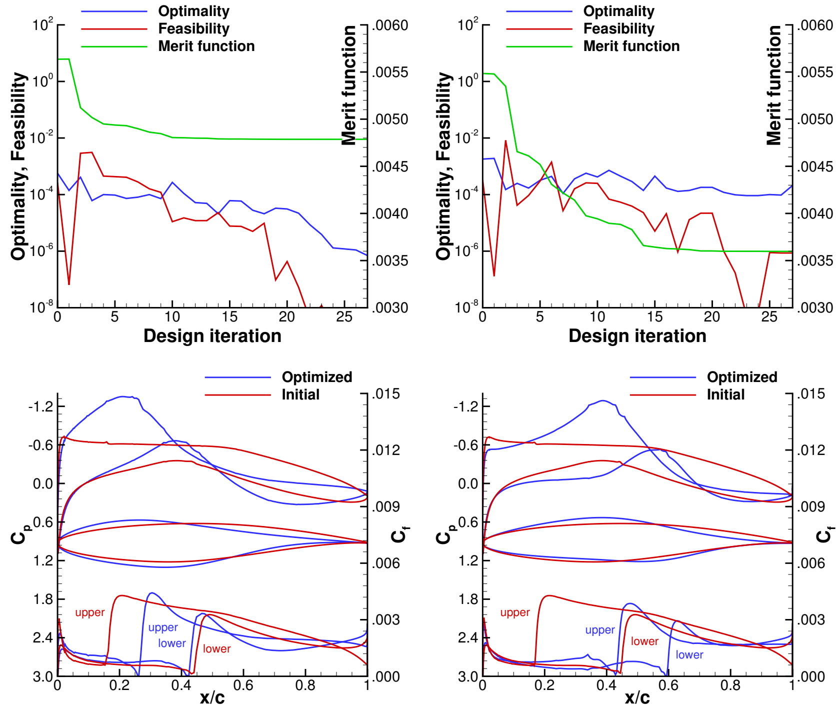

(a) L1 **(b) L2**

Fig. 5 Optimization convergence histories and cross-sectional profiles of the initial and optimized designs produced by drag minimizations with the baseline optimization problem (Equations 9-12) at the De Havilland Dash8-Q400 conditions with varying streamwise grid resolution.

There is a decrease in the transition length predicted by the transition model at the Dash8-Q400 design conditions, illustrated in Figure 5, relative to the transition length produced at the Cessna 172R conditions, which are presented in Figure 3. This decrease in transition length due to the increase in Reynolds number can help to explain the increased sensitivity of the optimizations to streamwise grid resolution, as finer streamwise grid spacing is required in order to maintain a similar resolution in the transition region to the Cessna 172R optimizations. Instead of delaying transition on the L1 grid, the optimization algorithm prioritizes developing strong adverse pressure gradients downstream of the transition location, which reduce the turbulent skin friction coefficient. This is similar to the behaviour of the drag minimization at the Cessna 172R design conditions on the L0 grid level (Figure 3a). The results suggest that the streamwise resolution of the grid must be increased as the Reynolds number increases in order to accurately resolve the large gradients in the transition region.

Similar to the designs in Figure 3, the designs in Figure 5 optimized using the baseline optimization problem produce excessively thin trailing edges. In order to improve manufacturability and to further explore the design space, drag minimizations are performed on the L2 grid level using the optimization problem with additional constraints introduced in Section III.A.1 (Equations 13-17). The optimized designs produced using the two optimization problems on the L2 grid level are presented in Figure 6. The results demonstrate that the optimization with the additional constraints produces a more aft-loaded design with increased trailing-edge thickness and a more gradual concave pressure recovery. However, opposite of the behaviour observed at the Cessna 172R design conditions (Figure 4), the more constrained design produces increased drag relative to the design optimized with the baseline optimization problem. Although the two optimized designs both delay transition to approximately 45% chord on the upper surface of the airfoil, the design optimized with the baseline optimization problem maintains a larger region of laminar flow on the lower surface. In addition, the steep pressure recovery produced by the baseline optimization problem decelerates the flow, producing decreased skin friction in the turbulent boundary layer, resulting in a decrease in skin friction drag relative to the more constrained design. Details of the aerodynamic performance of the initial blunt trailing-edge RAE2822 airfoil and two optimized designs on the L2 grid level are presented in Table 5. The results demonstrate that the optimization algorithm

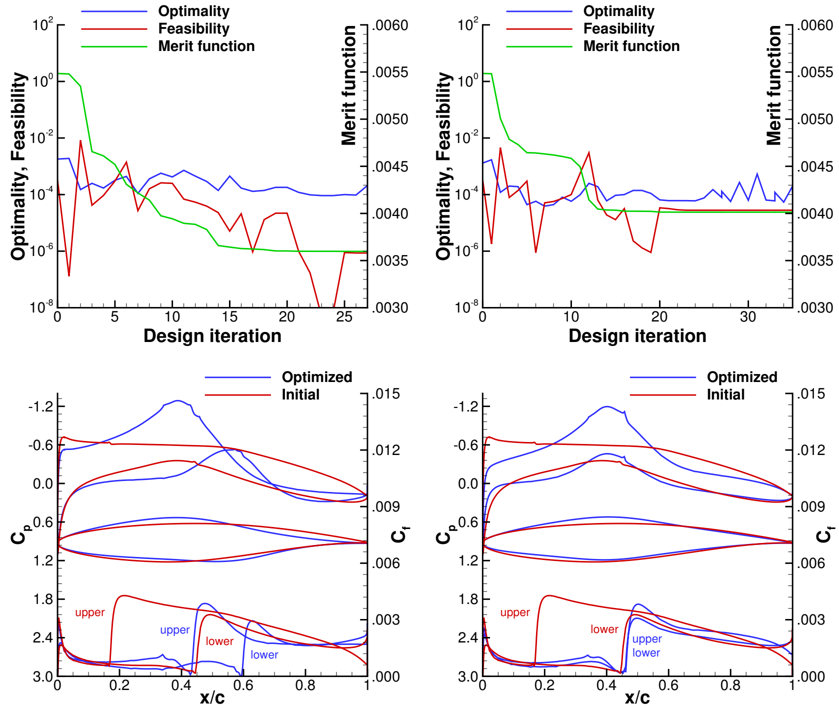

(a) Baseline Optimization Problem **(b) Additional Constraints**

Fig. 6 Optimization convergence histories and cross-sectional profiles of the initial and optimized designs produced by drag minimizations with the baseline (Equations 9-12) and more constrained optimization problem (Equations 13-17) at the De Havilland Dash8-Q400 conditions on the L2 grid level.

Table 5 Aerodynamic performance of the initial and optimized designs at the Dash8-Q400 conditions on the L2 grid level.

	C_d (cnts.)	C_l	C_m	L/D	aoa (deg.)
Initial	54.85	0.42	-0.074	76.438	1.329
Baseline Optimization Problem	35.85	0.42	-0.017	117.124	1.998
Additional Constraints	40.18	0.42	-0.074	104.521	0.722

was able to reduce drag by approximately 19 and 15 drag counts using the baseline and more constrained optimization problems, respectively. Therefore, adding a pitching moment constraint and more conservative thickness-to-chord ratio constraints incurs a drag penalty of 4 drag counts. Further investigation is required to determine if the design produced using the optimization problem with additional constraints is a local minima of the baseline optimization problem design space.

3. Boeing 737-800

To explore the performance of the free-transition optimization framework when applied to airfoil optimizations at design conditions similar to that of a single-aisle aircraft, lift-constrained drag minimizations were performed at the sweep-corrected Boeing 737-800 design conditions presented in Table 1. It is important to note again that because these optimizations are two-dimensional the effects of crossflow instabilities are not included. However, the purpose of this design problem is to evaluate the capabilities of the optimization algorithm to reduce Tollmien-Schlichting instabilities at the high Mach and Reynolds numbers typical of a single-aisle transport aircraft. Drag minimizations are performed on grids with streamwise grid resolutions representative of the L1 and L2 grid levels previously investigated, with the grid

Table 6 Structured multi-block O-grid dimensions for the two-dimensional optimizations at the sweep-corrected Boeing 737-800 design conditions (see Table 1).

grid level	chord x off-wall nodes	avg/max $\Delta s \times 10^{-6}$ (chord)	avg/max $y+$
L1	561x121	0.54 / 0.60	0.25 / 0.50
L2	1121x121	"	"

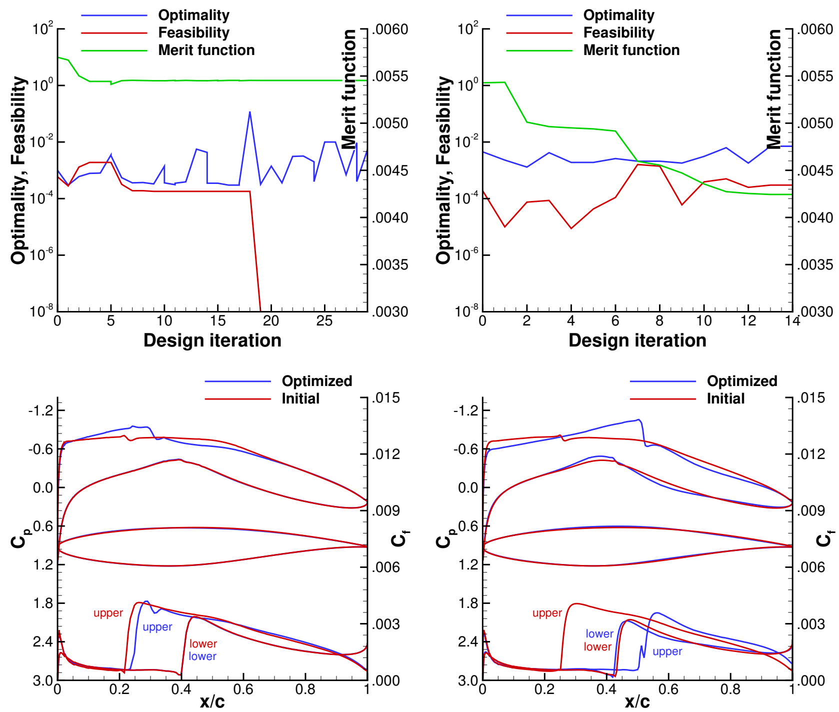

(a) L1 **(b) L2**

Fig. 7 Optimization convergence histories and cross-sectional profiles of the initial and optimized designs produced by drag minimizations with the baseline optimization problem (Equations 9-12) at the sweep-corrected Boeing 737-800 conditions with varying streamwise grid resolution.

details presented in Table 6. Optimizations are performed using the baseline optimization problem (Equations 9-12).

The results, which are presented in Figure 7, demonstrate that the grid-resolution requirements identified in the Cessna 172R and De Havilland Dash8-Q400 drag minimizations are amplified at the higher Mach and Reynolds numbers of the Boeing 737-800 conditions. Specifically, as the Reynolds number increases the transition region decreases further. Therefore, the drag minimization on the L1 grid (Figure 7a) fails to significantly move the transition fronts aft as the effective grid resolution in the transition region decreases. The optimization algorithm appears to encounter difficulty trading a decrease in viscous drag associated with delaying boundary-layer transition with the increase in wave drag associated with the development of a favourable pressure gradient to delay transition. This is also demonstrated by the optimization history in Figure 7a, which illustrates that convergence of the merit function has stalled. The performance of the optimization algorithm improves significantly going from the L1 to the L2 grid level. The optimization algorithm successfully produces a favourable pressure gradient on the upper surface of the airfoil to delay transition and in the process produces a shock wave at approximately 50% chord. The results in Figure 7b demonstrate that provided enough grid resolution in the transition region the optimization algorithm is able to successfully trade a decrease in viscous drag produced by delaying boundary-layer transition with an increase in wave drag.

The aerodynamic performance metrics for the initial and optimized design on the L2 grid level are presented in Table 7, including drag breakdowns for the initial and optimized designs. The results demonstrate that the optimized

Table 7 Aerodynamic performance of the initial and optimized designs at the sweep-corrected Boeing 737-800 conditions on the L2 grid level.

	C_d (cnts.)	$C_{d,p}$	$C_{d,f}$	C_l	C_m	L/D	aoa (deg.)
Initial	54.33	18.62	35.71	0.50	-0.086	92.018	1.291
Optimized	42.49	13.30	29.19	0.50	-0.088	117.519	1.133

design with a larger extent of laminar flow on the upper surface of the airfoil produces decreased skin friction drag as well as a net decrease in pressure drag, as the reduction in the pressure component of viscous drag is larger than the increase in wave drag.

B. Infinite Swept Wing Optimization

An infinite swept wing optimization was performed at design conditions similar to a transonic strut-braced wing aircraft [11]. The goal of the drag minimization at this design condition is to evaluate the ability of the optimization algorithm to delay both Tollmien-Schlichting and stationary crossflow instabilities. Specifically, a lift-constrained drag minimization was conducted using an initial geometry consisting of an RAE2822 airfoil extruded with a 30 degree sweep. The infinite swept wing O-grid consists of 857, 103, and 11 nodes in the streamwise, off-wall, and spanwise directions, respectively, with an average $y+$ value of 0.50. Design conditions were specified as a Mach number of 0.80, Reynolds number of 12.12×10^6, turbulence intensity of 0.10%, surface roughness of 1μinch, with a target cruise lift coefficient of 0.56. An optimization problem similar to the baseline optimization problem (Equations 9-12) was used for the infinite swept wing optimization; however, to expand the design space the cross-sectional area constraint was removed and more conservative thickness bounds were placed on the FFD design variable pairs. The infinite swept wing optimization problem is defined as follows,

$$\min_{\boldsymbol{X}} \quad C_D(\boldsymbol{Q}, \boldsymbol{X}), \tag{18}$$

$$\text{s.t.} \quad C_L = 0.56, \tag{19}$$

$$t/c \geq 0.85 t/c_{\text{init}}. \tag{20}$$

Similar to the airfoil optimizations, 6 streamwise FFD design variables are applied to each of the upper and lower surfaces, with the infinite swept wing root and tip design variables constrained to be equal and the leading- and trailing-edge design variables constrained to move symmetrically, for a total of 10 effective geometric design variables plus angle of attack.

The results from the drag minimization are presented in Figure 8. The optimization history illustrated in Figure 8a demonstrates that the optimization algorithm successfully reduces drag by approximately 12 counts. The optimized cross-sectional profiles in Figure 8b demonstrate that the optimization algorithm produces near-zero pressure gradients on the upper and lower surfaces of the wing, which delay transition to 60% and 40% chord, respectively. While the initial design already featured a near-zero upper surface pressure gradient, it is important to note that the optimization algorithm has removed the favourable pressure gradient on the lower surface of the wing to prevent the growth of crossflow instabilities and therefore delay transition on the lower surface. The optimization algorithm produced these near-zero pressure gradients on the upper and lower surfaces by reducing the wing thickness and moving the aerodynamic loading aft.

The integrated forces for the initial and optimized infinite swept wing designs are presented in Table 8. The results demonstrate that the pressure and skin friction drag components account for approximately 60% and 40% of the total drag reduction, respectively. The relatively larger reduction in pressure drag can be explained by Figure 8b, which illustrates that the optimized design simultaneously reduces the strength of the shock while increasing the laminar extent of the boundary layer, which the optimizer achieved by reducing the maximum thickness-to-chord ratio and the cross-sectional area. Future optimizations will investigate this optimization problem with a more conservative cross-sectional area constraint, similar to that used in the airfoil optimizations.

IV. Conclusions

The SA-sLM2015 smooth local correlation-based transition model is fully coupled with a Newton-Krylov RANS-based flow solver and discrete-adjoint gradient-based optimization algorithm, with the analytical partial derivatives and

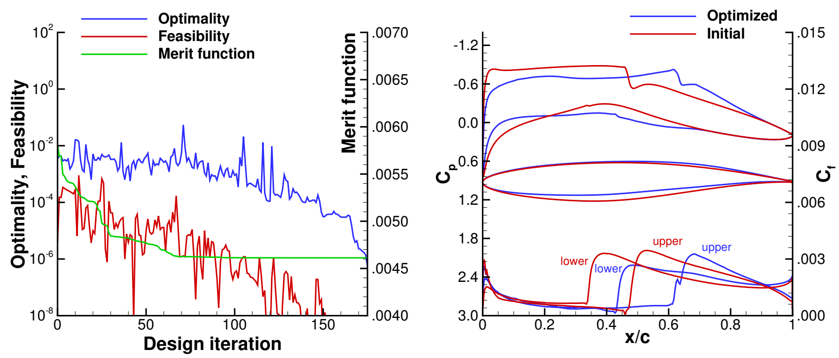

(a) Optimization history **(b) Cross-sectional profiles**

Fig. 8 Infinite swept wing drag minimization at the transonic strut-braced wing aircraft design conditions.

Table 8 Aerodynamic performance of the initial and optimized infinite swept wing designs at the transonic strut-braced wing aircraft design conditions.

	C_D (cnts.)	$C_{D,p}$	$C_{D,f}$	C_L	C_M	L/D	aoa (deg.)
Initial	58.10	25.97	32.13	0.56	-0.23	96.38	2.10
Optimized	46.12	18.99	27.13	0.56	-0.28	121.42	0.94

gradients verified using finite-difference and complex-step approximations. The free-transition optimization framework is applied to lift-constrained drag minimizations of airfoils and an infinite swept wing geometry. Airfoil optimizations are performed at design conditions ranging from a light aircraft to a single-aisle aircraft, with the infinite swept wing optimized at design conditions similar to a transonic strut-braced wing aircraft.

The results demonstrate that increasing the streamwise resolution, and therefore better resolving the large gradients in the boundary-layer transition region, improves the capability of the optimization algorithm to delay boundary-layer transition. Airfoil optimizations at the Cessna 172R light aircraft design conditions demonstrate that the design space is multi-modal, with the optimization algorithm producing (at least) two distinct local minima: one with a thin, reflexed trailing edge and steep pressure recovery regions, the other similar to the design produced by Rashad and Zingg [32] at the same design conditions featuring more aft loading. The latter design outperforms the former, demonstrating the importance of addressing multimodality for such design problems.

As the transition length decreases with increasing Reynolds number, finer streamwise mesh spacings are required to maintain sufficient mesh resolution to adequately resolve the streamwise gradients in the transition region. Despite increasing the streamwise grid resolution, drag minimizations at the De Havilland Dash8-Q400 and sweep-corrected Boeing 737-800 design conditions fail to delay boundary-layer transition as far aft as the stability-analysis based optimization framework developed by Rashad and Zingg [32]. However, optimizations at the sweep-corrected Boeing 737-800 design conditions demonstrate that the optimization algorithm is able to successfully trade a decrease in viscous drag associated with delaying boundary-layer transition with an increase in wave drag. The decrease in the pressure component of viscous drag due to the increased laminar extent of the boundary layer is more significant than the increase in wave drag, resulting in a net decrease in both pressure and skin friction drag. The drag minimization of the infinite swept wing geometry at the transonic strut-braced wing aircraft design conditions demonstrates that the optimization algorithm successfully delays both Tollmien-Schlichting and stationary crossflow instabilities.

Future work will investigate methods for reducing the streamwise grid requirements of the free-transition gradient-based optimization framework, and the impact of increasing the number of design variables on the ability of the optimization algorithm to delay boundary-layer transition.

Acknowledgments

This work was partially funded by the NASA Transformational Tools and Technologies (TTT) and Advanced Air Transport Technology (AATT) projects, the Natural Sciences and Engineering Research Council (NSERC), and the

University of Toronto. Computations were performed on the Niagara supercomputer at the SciNet HPC Consortium, a part of Compute Canada. The authors gratefully acknowledge the input and support provided by Timothy Chau, Dr. Cetin Kiris, and the LAVA team.

References

[1] Green, J. E., "Civil aviation and the environment: the next frontier for the aerodynamicist," *Aeronautical Journal*, Vol. 110, No. 1110, 2006, pp. 469–486. doi:https://doi.org/10.1017/S0001924000001378.

[2] Bushnell, D. M., "Overview of aircraft drag reduction technology," *AGARD Report 786 (Special Course on Skin Friction Drag Reduction)*, 1992.

[3] Malik, M. R., Crouch, J. D., Saric, W. S., Lin, J. C., and Whalen, E. A., "Application of Drag Reduction Techniques to Transport Aircraft," *In Encyclopedia of Aerospace Engineering (eds R. Blockley and W. Shyy)*, 2015. doi:https://doi.org/10.1002/9780470686652.eae1013.

[4] Crouch, J. D., "Boundary-Layer Transition Prediction for Laminar Flow Control," *45th AIAA Fluid Dynamics Conference*, AIAA Paper 2015-2472, Dallas, TX, 2015. doi:https://doi.org/10.2514/6.2015-2472.

[5] Campbell, R. L., and Lynde, M. N., "Natural Laminar Flow Design for Wings with Moderate Sweep," *34th AIAA Applied Aerodynamics Conference*, AIAA Paper 2016-4326, Washington D.C., 2016. doi:https://doi.org/10.2514/6.2016-4326.

[6] Lynde, M. N., Campbell, R. L., Rivers, M. B., Viken, S. A., Chan, D. T., Watkins, N. A., and Goodliff, S. L., "Preliminary Results from an Experimental Assessment of a Natural Laminar Flow Design Method," *2019 AIAA Aerospace Sciences Meeting*, AIAA Paper 2019-2298, 2019. doi:https://doi.org/10.2514/6.2019-2298.

[7] Lynde, M. N., Campbell, R. L., and Viken, S. A., "Additional Findings from the Common Research Model Natural Laminar Flow Wind Tunnel Test," *AIAA Aviation 2019 Forum*, AIAA Paper 2019-3292, 2019. doi:https://doi.org/10.2514/6.2019-3292.

[8] Kenway, G. K. W., and Martins, J. R. R. A., "Multipoint High-Fidelity Aerostructural Optimization of a Transport Aircraft Configuration," *Journal of Aircraft*, Vol. 51, No. 1, 2014, pp. 144–160. doi:https://doi.org/10.2514/1.C032150.

[9] Reist, T. A., and Zingg, D. W., "High-Fidelity Aerodynamic Shape Optimization of a Lifting-Fuselage Concept for Regional Aircraft," *Journal of Aircraft*, Vol. 54, No. 3, 2016, pp. 1085–1097. doi:https://doi.org/10.2514/1.C033798.

[10] Reist, T. A., Zingg, D. W., Rakowitz, M., Potter, G., and Banerjee, S., "Multifidelity Optimization of Hybrid Wing-Body Aircraft with Stability and Control Requirements," *Journal of Aircraft*, Vol. 56, No. 2, 2018, pp. 442–456. doi:https://doi.org/10.2514/1.C034703.

[11] Chau, T., and Zingg, D. W., "Aerodynamic Design Optimization of a Transonic Strut-Braced-Wing Regional Aircraft," *Journal of Aircraft*, Vol. 0, No. 0, 2021, pp. 1–19. doi:https://doi.org/10.2514/1.C036389.

[12] Drela, M., "Design and optimization method for multi-element airfoils," *Aerospace Design Conference*, 1993. doi:https://doi.org/10.2514/6.1993-969.

[13] Dodbele, S. S., "Design optimization of natural laminar flow bodies in compressible flow," *Journal of aircraft*, Vol. 29, No. 3, 1992, pp. 343–347. doi:https://doi.org/10.2514/3.46167.

[14] Green, B. E., Whitesides, J. L., Campbell, R. L., and Mineck, R. E., "Method for the Constrained Design of Natural Laminar Flow Airfoils," *Journal of Aircraft*, Vol. 34, No. 6, 1997, pp. 706–712. doi:https://doi.org/10.2514/2.2248.

[15] Pralits, J. O., "Optimal design of natural and hybrid laminar flow control on wings," Ph.D. thesis, Department of Mechanics, Royal Institute of Technology, Stockholm, Sweden, 2003.

[16] Kroo, I., and Sturdza, P., "Design-Oriented Aerodynamic Analysis for Supersonic Laminar Flow Wings," *41st Aerospace Sciences Meeting and Exhibit*, 2003. doi:https://doi.org/10.2514/6.2003-774.

[17] Amoignon, O., Pralits, J., Hanifi, A., Berggren, M., and Henningson, D., "Shape Optimization for Delay of Laminar-Turbulent Transition," *AIAA Journal*, Vol. 44, No. 5, 2006, pp. 1009–1024. doi:https://doi.org/10.2514/1.12431.

[18] Zhao, K., Gao, Z., and Huang, J., "Robust Design of Natural Laminar Flow Supercritical Airfoil by Multi-Objective Evolution Method," *Applied Mathematics and Mechanics*, Vol. 35, No. 2, 2014, pp. 191–202. doi:https://doi.org/10.1007/s10483-014-1783-6.

[19] Robitaille, M., Mosahebi, A., and Laurendeau, E., "Design of adaptive transonic laminar airfoils using the γ-$\tilde{Re}_{\theta t}$ transition model," *Aerospace Science and Technology*, Vol. 46, 2015, pp. 60–71. doi:https://doi.org/10.1016/j.ast.2015.06.027.

[20] Zhang, Y., Fang, X., Chen, H., Fu, S., Duan, Z., and Zhang, Y., "Supercritical natural laminar flow airfoil optimization for regional aircraft wing design," *Aerospace Science and Technology*, Vol. 43, 2015, pp. 152–164. doi:https://doi.org/10.1016/j.ast.2015.02.024.

[21] Han, Z.-H., Chen, J., Zhang, K.-S., Xu, Z.-M., Zhu, Z., and Song, W.-P., "Aerodynamic Shape Optimization of Natural-Laminar-Flow Wing Using Surrogate-Based Approach," *AIAA Journal*, Vol. 56, No. 7, 2018, pp. 2579–2593. doi:https://doi.org/10.2514/1.J056661.

[22] Tang, Z., Chen, Y., and Zhang, L., "Natural laminar flow shape optimization in transonic regime with competitive Nash game strategy," *Applied Mathematical Modelling*, Vol. 48, 2017, pp. 534–547. doi:https://doi.org/10.1016/j.apm.2017.04.012.

[23] Hollom, J., and Qin, N., "Uncertainty analysis and robust shape optimisation for laminar flow aerofoils," *The Aeronautical Journal*, Vol. 125, No. 1284, 2021, pp. 365–388. doi:https://doi.org/10.1017/aer.2020.63.

[24] Sabater, C., Bekemeyer, P., and Görtz, S., "Robust Design of Transonic Natural Laminar Flow Wings under Environmental and

Operational Uncertainties," *AIAA Scitech 2021 Forum*, 2021. doi:10.2514/6.2021-0071.
[25] Driver, J., and Zingg, D. W., "Numerical Aerodynamic Optimization Incorporating Laminar-Turbulent Transition Prediction," *AIAA Journal*, Vol. 45, No. 8, 2007, pp. 1810–1818. doi:https://doi.org/10.2514/1.23569.
[26] Drela, M., and Giles, M. B., "Viscous-inviscid analysis of transonic and low Reynolds number airfoils," *AIAA Journal*, Vol. 25, No. 10, 1987, pp. 1347–1355. doi:https://doi.org/10.2514/3.9789.
[27] Spalart, P. R., and Allmaras, S. R., "A One-Equation Turbulence Model for Aerodynamic Flows," *30th AIAA Aerospace Sciences Meeting and Exhibit*, AIAA Paper 092-0439, Reno, Nevada, United States 1992. doi:https://doi.org/10.2514/6.1992-439.
[28] Liebeck, R. H., "A Class of Airfoils Designed for High Lift in Incompressible Flow," *Journal of Aircraft*, Vol. 10, No. 10, 1973, pp. 610–617. doi:https://doi.org/10.2514/3.60268.
[29] Zingg, D. W., "An Approach to the Design of Airfoils with High Lift to Drag Ratios," Master's thesis, University of Toronto, Toronto, Ontario, Canada, 1981.
[30] Lee, J., and Jameson, A., "Natural-Laminar-Flow Airfoil and Wing Design by Adjoint Method and Automatic Transition Prediction," *47th AIAA Aerospace Sciences Meeting and Exhibit*, AIAA Paper 2009-897, Orlando, Florida, January, 2009. doi:https://doi.org/10.2514/6.2009-897.
[31] Baldwin, B., and Lomax, H., "Thin-layer approximation and algebraic model for separated turbulent flows," *16th Aerospace Sciences Meeting*, 1978. doi:https://doi.org/10.2514/6.1978-257.
[32] Rashad, R., and Zingg, D. W., "Aerodynamic shape optimization for natural laminar flow using a discrete-adjoint approach," *AIAA Journal*, Vol. 54, No. 11, 2016, pp. 3321–3337. doi:https://doi.org/10.2514/1.J054940.
[33] Rashad, R., "High-Fidelity Aerodynamic Shape Optimization for Natural Laminar Flow," Ph.D. thesis, University of Toronto, Toronto, Ontario, Canada, 2016.
[34] Shi, Y., Mader, C. A., He, S., Halila, G. L. O., and Martins, J. R. R. A., "Natural Laminar-Flow Airfoil Optimization Design Using a Discrete Adjoint Approach," *AIAA Journal*, Vol. 58, No. 11, 2020, pp. 4702–4722. doi:https://doi.org/10.2514/1.J058944.
[35] Fujino, M., Yoshizaki, Y., and Kawamura, Y., "Natural-Laminar-Flow Airfoil Development for a Lightweight Business Jet," *Journal of Aircraft*, Vol. 40, No. 4, 2003, pp. 609–615. doi:https://doi.org/10.2514/2.3145.
[36] Shi, Y., Mader, C. A., and Martins, J. R. R. A., "Natural laminar flow wing optimization using a discrete adjoint approach," *Structural and Multidisciplinary Optimization*, Vol. 64, No. 2, 2021, pp. 541–562. doi:https://doi.org/10.1007/s00158-021-02936-w.
[37] Zhu, M., and Qin, N., "Balancing Laminar Extension and Wave Drag for Transonic Swept Wings," *AIAA Journal*, Vol. 59, No. 5, 2021, pp. 1660–1672. doi:https://doi.org/10.2514/1.J059914.
[38] Poll, D., "Transition in the Infinite Swept Attachment Line Boundary Layer," *Aeronautical Quarterly*, Vol. 30, No. 4, 1979, pp. 607–629. doi:https://doi.org/10.1017/S0001925900008763.
[39] Fan, Z., Yu, X., Qin, N., and Zhu, M., "Benefit Assessment of Low-Sweep Transonic Natural Laminar Flow Wing for Commercial Aircraft," *Journal of Aircraft*, Vol. 0, No. 0, 0, pp. 1–8. doi:https://doi.org/10.2514/1.C036138.
[40] Krumbein, A., Krimmelbein, N., and Schrauf, G., "Automatic transition prediction in hybrid flow solver, part 1: Methodology and sensitivities," *Journal of Aircraft*, Vol. 46, No. 4, 2009, pp. 1176–1190. doi:https://doi.org/10.2514/1.39736.
[41] Krumbein, A., Krimmelbein, N., and Schrauf, G., "Automatic transition prediction in hybrid flow solver, part 2: Practical application," *Journal of Aircraft*, Vol. 46, No. 4, 2009, pp. 1191–1199. doi:https://doi.org/10.2514/1.39738.
[42] Langtry, R. B., and Menter, F. R., "Correlation-based transition modeling for unstructured parallelized computational fluid dynamics codes," *AIAA Journal*, Vol. 47, No. 12, 2009, pp. 2894–2906. doi:https://doi.org/10.2514/1.42362.
[43] Khayatzadeh, P., and Nadarajah, S. K., "Aerodynamic Shape Optimization via Discrete Viscous Adjoint Equations for the k-ω SST Turbulence and γ-$\tilde{Re}_{\theta t}$ Transition Models," *49th AIAA Aerospace Sciences Meeting including the New Horizons Forum and Aerospace Exposition*, AIAA Paper 2011-1247, Orlando, Florida, January, 2011. doi:https://doi.org/10.2514/6.2011-1247.
[44] Khayatzadeh, P., and Nadarajah, S. K., "Aerodynamic Shape Optimization of Natural Laminar Flow (NLF) Airfoils," *50th AIAA Aerospace Sciences Meeting including the New Horizons Forum and Aerospace Exposition*, AIAA Paper 2012-0061, Nashville, Tennessee, January, 2012. doi:https://doi.org/10.2514/6.2012-61.
[45] Halila, G. L. O., Martins, J. R. R. A., and Fidkowski, K. J., "Adjoint-Based Aerodynamic Shape Optimization Including Transition to Turbulence Effects," *Aerospace Science and Technology*, Vol. 107, 2020, pp. 1–15. doi:https://doi.org/10.1016/j.ast.2020.106243.
[46] Coder, J. G., and Maughmer, M. D., "Computational fluid dynamics compatible transition modeling using an amplification factor transport equation," *AIAA Journal*, Vol. 52, No. 11, 2014, pp. 2506–2512. doi:https://doi.org/10.2514/1.J052905.
[47] Yang, Z., and Mavriplis, D. J., "Discrete Adjoint Formulation for Turbulent Flow Problems with Transition Modelling on Unstructured Meshes," *AIAA Scitech 2019 Forum*, 2019. doi:10.2514/6.2019-0294.
[48] Mavriplis, D. J., Yang, Z., and Anderson, E. M., "Adjoint Based Optimization of a Slotted Natural Laminar Flow Wing for Ultra Efficient Flight," *AIAA Scitech 2020 Forum*, 2020. doi:https://doi.org/10.2514/6.2020-1292.
[49] Menter, F. R., Smirnov, P. E., Liu, T., and Avancha, R., "A One-Equation Local Correlation-Based Transition Model," *Flow, Turbulence and Combustion*, Vol. 95, 2015, pp. 583–619. doi:https://doi.org/10.1007/s10494-015-9622-4.
[50] Kaya, H., and Tuncer, I. H., "Discrete Adjoint-Based Aerodynamic Shape Optimization Framework for Natural Laminar Flows," *AIAA Journal*, 2021. doi:https://doi.org/10.2514/1.J059923.
[51] Piotrowski, M. G. H., and Zingg, D. W., "Smooth Local Correlation-based Transition Model for the Spalart-Allmaras Turbulence

Model," *AIAA Journal*, Vol. 59, No. 2, 2021, pp. 474–492. doi:https://doi.org/10.2514/1.J059784.

[52] Piotrowski, M. G. H., and Zingg, D. W., "Compressibility Corrections to Extend a Smooth Local Correlation-Based Transition Model to Transonic Flows," *AIAA Journal*, Submitted July, 2021.

[53] Piotrowski, M. G. H., and Zingg, D. W., "Numerical Behaviour of a Smooth Local Correlation-based Transition Model in a Newton-Krylov Flow Solver," *AIAA Scitech 2022 Forum*, 2022.

[54] Hicken, J. E., and Zingg, D. W., "Aerodynamic Optimization Algorithm with Integrated Geometry Parameterization and Mesh Movement," *AIAA Journal*, Vol. 48, No. 2, 2010, pp. 400–413. doi:https://doi.org/10.2514/1.44033.

[55] Gagnon, H., and Zingg, D. W., "Two-Level Free-Form and Axial Deformation for Exploratory Aerodynamic Shape Optimization," *AIAA Journal*, Vol. 53, No. 7, 2015, pp. 2015–2026. doi:10.2514/1.J053575.

[56] Lee, C., Koo, D., and Zingg, D. W., "Comparison of B-spline Surface and Free-form Deformation Geometry Control Methods for Aerodynamic Shape Optimization," *AIAA Journal*, Vol. 55, No. 1, 2017, pp. 228–240. doi:https://doi.org/10.2514/1.J055102.

[57] Hicken, J. E., and Zingg, D. W., "Parallel Newton-Krylov solver for the Euler equations discretized using simultaneous approximation terms," *AIAA Journal*, Vol. 46, No. 11, 2008, pp. 2773–2786. doi:https://doi.org/10.2514/1.34810.

[58] Osusky, M., and Zingg, D. W., "Parallel Newton-Krylov-Schur Flow Solver for the Navier-Stokes Equations," *AIAA Journal*, Vol. 51, No. 12, 2013, pp. 2833–2851. doi:https://doi.org/10.2514/1.J052487.

[59] Osusky, L., Buckley, H. P., Reist, T. A., and Zingg, D. W., "Drag Minimization Based on the Navier-Stokes Equations Using a Newton-Krylov Approach," *AIAA Journal*, Vol. 53, No. 6, 2015, pp. 1555–1577. doi:https://doi.org/10.2514/1.J053457.

[60] Reist, T. A., Koo, D., Zingg, D. W., Bochud, P., Castonguay, P., and Leblond, D., "Cross Validation of Aerodynamic Shape Optimization Methodologies for Aircraft Wing-Body Optimization," *AIAA Journal*, Vol. 58, No. 6, 2020, pp. 2581–2595. doi:https://doi.org/10.2514/1.J059091.

[61] Osusky, M., Boom, P. D., and Zingg, D. W., "Results from the Fifth AIAA Drag Prediction Workshop obtained with a parallel Newton-Krylov-Schur flow solver discretized using summation-by-parts operators," *31st AIAA Applied Aerodynamics Conference*, AIAA 2013-2511, 2013. doi:10.2514/6.2013-2511.

[62] Swanson, R. C., and Turkel, E., "On central-difference and upwind schemes," *Journal of Computational Physics*, Vol. 101, 1992, pp. 292–306. doi:https://doi.org/10.1016/0021-9991(92)90007-L.

[63] Medida, S., and Baeder, J. D., "Application of the Correlation-based γ-$\tilde{Re}_{\theta t}$ Transition Model to the Spalart-Allmaras Turbulence Model," *20th AIAA Computational Fluid Dynamics Conference*, AIAA Paper 2011-3979, Honolulu, HI, 2011. doi:https://doi.org/10.2514/6.2011-3979.

[64] Langtry, R. B., Sengupta, K., Yeh, D. T., and Dorgan, A. J., "Extending the γ-$\tilde{Re}_{\theta t}$ Correlation based Transition Model for Crossflow Effects," *45th AIAA Fluid Dynamics Conference*, AIAA Paper 2015-2474, 2015. doi:https://doi.org/10.2514/6.2015-2474.

[65] Hicken, J. E., and Zingg, D. W., "A Simplified and flexible variant of GCROT for solving nonsymmetric linear systems," *SIAM Journal on Scientific Computing*, Vol. 32, No. 3, 2010, pp. 1672–1694. doi:https://doi.org/10.1137/090754674.

[66] Gill, P. E., Murray, W., and Saunders, M. A., "SNOPT: an SQP algorithm for large-scale Constrained Optimization," *SIAM Journal on Optimization*, Vol. 12, No. 4, 2002, pp. 979–1006. doi:https://doi.org/10.1137/S0036144504446096.

[67] Hicken, J. E., "Efficient algorithms for future aircraft design: contributions to aerodynamic shape optimization," Ph.D. thesis, Graduate Department of Aerospace Science and Engineering, University of Toronto, 2009.

[68] Osusky, L., "A Numerical Methodology for Aerodynamic Shape Optimization in Turbulent Flow Enabling Large Geometric Variation," Ph.D. thesis, Graduate Department of Aerospace Science and Engineering, University of Toronto, 2014.

[69] Chernukhin, O., and Zingg, D. W., "Multimodality and Global Optimization in Aerodynamic Design," *AIAA Journal*, Vol. 51, No. 6, 2013, pp. 1342–1354. doi:https://doi.org/10.2514/1.J051835.

[70] Streuber, G. M., and Zingg, D. W., "Evaluating the Risk of Local Optima in Aerodynamic Shape Optimization," *AIAA Journal*, Vol. 59, No. 1, 2021, pp. 75–87. doi:https://doi.org/10.2514/1.J059826.